AIP | Applied Physics Letters

Frequency dependence of the maximum operating temperature for quantum-cascade lasers up to 5.4 THz

M. Wienold, B. Röben, X. Lü, G. Rozas, L. Schrottke, K. Biermann, and H. T. Grahn

Citation: Applied Physics Letters **107**, 202101 (2015); doi: 10.1063/1.4935942
View online: http://dx.doi.org/10.1063/1.4935942
View Table of Contents: http://scitation.aip.org/content/aip/journal/apl/107/20?ver=pdfcov
Published by the AIP Publishing

Frequency dependence of the maximum operating temperature for quantum-cascade lasers up to 5.4 THz

M. Wienold,[1,2,3] B. Röben,[1] X. Lü,[1] G. Rozas,[1] L. Schrottke,[1] K. Biermann,[1] and H. T. Grahn[1,a)]
[1]*Paul-Drude-Institut für Festkörperelektronik, Hausvogteiplatz 5–7, 10117 Berlin, Germany*
[2]*Humboldt Universität zu Berlin, Institut für Physik, Newtonstr. 15, 12489 Berlin, Germany*
[3]*Deutsches Zentrum für Luft und Raumfahrt, Rutherfordstr. 2, 12489 Berlin, Germany*

(Received 10 September 2015; accepted 5 November 2015; published online 16 November 2015)

We report on the observation of an approximately linear reduction in the maximum operating temperature with an increasing emission frequency for terahertz quantum-cascade lasers between 4.2 and 5.4 THz. These lasers are based on the same design type, but vary in period length and barrier height for the cascade structure. The sample emitting at the highest frequency around 5.4 THz can be operated in pulsed mode up to 56 K. We identify an additional relaxation channel for electrons by longitudinal optical phonon scattering from the upper to the lower laser level and increasing optical losses toward higher frequencies as major processes, leading to the observed temperature behavior. © *2015 AIP Publishing LLC*. [http://dx.doi.org/10.1063/1.4935942]

Terahertz quantum-cascade lasers (THz QCLs) are semiconductor laser sources for the THz range,[1] which are employed for several scientific applications in the fields of spectroscopy, imaging, and astronomy.[2–5] Without the assistance of a magnetic field, the frequency range for which laser operation has been reported ranges from 1.2 to 5.2 THz.[6,7] In this work, we report on a THz QCL operating around 5.4 THz, extending the previous operating range on the high-frequency side. THz QCLs emitting above 5 THz are of interest for high-resolution spectroscopy of gaseous species as well as of shallow donor transitions in isotopically enriched semiconductors. One example for silicon in the 5.1–5.7 THz range is the 1 s(T_2) → 2p_0 transition of Si:P at 5.417 THz.[8,9]

THz QCLs operate currently at cryogenic temperatures only, the highest reported temperatures being 199 and 129 K for pulsed and continuous-wave operation, respectively.[10,11] The detailed reasons for the limitation to low operating temperatures are still under discussion.[10,12–14] By evaluating the temperature performance for a larger series of samples in the range of 4.2–5.4 THz, we find clear evidence that additional relaxation of electrons by longitudinal optical (LO) phonon scattering from the upper to the lower laser level is the major limiting mechanism for the maximum operating temperature of these lasers.

The employed active-region design has been originally developed for emission around 4.75 THz and relies on a bound-to-continuum scheme with a vertical optical transition and a LO phonon-assisted injection.[15] Figure 1(a) depicts a band structure diagram at 5 kV/cm and Fig. 1(b) a map of the calculated gain. Details of the self-consistent simulation routine are found in Refs. 16 and 17. The simulations are performed for a temperature parameter of 50 K corresponding to an energy parameter $E_a = 4.3$ meV as defined in Ref. 16. The strong optical gain in the region of 4.2–5.3 THz is mainly generated by electronic transitions between the states labeled *up* and *lo* in Fig. 1(a). Electrons are transferred by LO-phonon emission from a miniband into one of the states labeled *i* and *j* and subsequently injected into the upper laser level (*up*) by resonant tunneling. One particular difference to alternative design approaches such as in Ref. 18 is the creation of a space charge region around the injection barrier at 250 nm in Fig. 1(a). This space charge region results in a self-alignment of the injector states and the upper laser level, which yields an efficient injection by resonant tunneling over a larger bias range. Figure 1(c) illustrates the impact of a variation of the relative period length L/L_0 (where all layers experience the same relative change in thickness) and a variation of the Al content x on the frequency of the gain maximum. For changing L/L_0 in the range $0.93 \leq L/L_0 \leq 1.07$, the calculated position of the gain maximum varies between 5.4 and 4.3 THz, while a shift between 4.6 and 5.0 THz is obtained for varying the Al content in the barriers between 20% and 30%. We found no evidence of such a strong unintentional wafer-to-wafer variation of the barrier composition for our growth system by means of secondary-ion mass spectroscopy. However, a variation of the relative period length in the range of several percent is typical for the employed molecular-beam epitaxy (MBE), in particular, in the absence of *in-situ* thickness control.

Wafers have been grown by MBE starting with a 700 nm-thick GaAs layer Si-doped with a density of 2×10^{18} cm^{-3} followed by 88 active-region periods [cf. Fig. 1(a)] adding up to a total thickness of 11 μm. For sample characterization, Fabry-Pérot QCLs based on wet-etched single-plasmon waveguides[1,21] have been fabricated. For the sample emitting at 5.4 THz, x-ray diffraction data for a center reference position on the wafer revealed a thickness deviation of −5.4% as compared to the nominal design shown in Fig. 1(a). We ascribe this deviation to a calibration error of the Ga flux rate, which is expected to affect the thickness of the quantum wells and barriers in almost the same manner. Due to the reduced Ga flux, we estimate the average Al content x in the barriers to be increased to 0.26 as compared to the nominal value of 0.25. By accounting for both of these deviations in the simulations, we obtain a shift of the gain maximum from 4.8 toward

a)Electronic mail: htgrahn@pdi-berlin.de

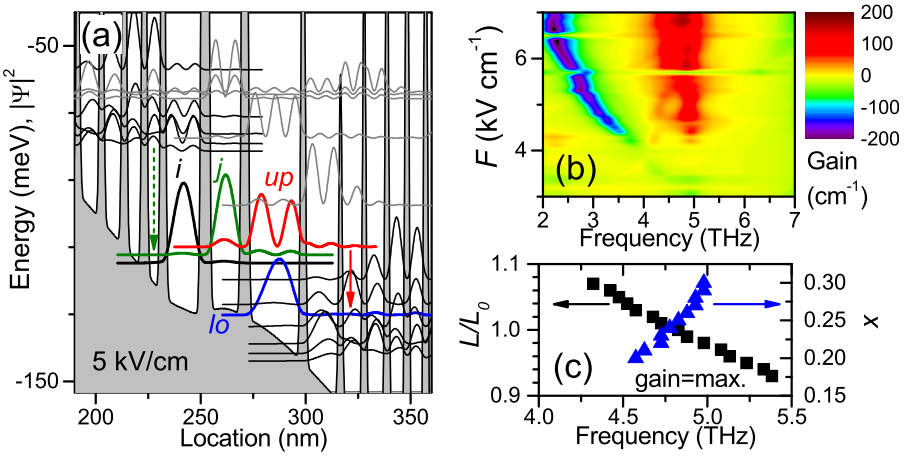

FIG. 1. (a) Calculated band structure diagram of the active-region period with $Al_xGa_{1-x}As$ ($x = 0.25$) barriers at 5 kV/cm, including an interface grading parameter of 1.6 monolayers.[19,20] *i* and *j*: injector states; *up*: upper laser level; *lo*: lower laser level. The dashed arrow indicates the LO phonon-assisted transition and the solid arrow the laser transition. The nominal layer sequence of a single period in nm is given by **3.0**/25.4/**1.7**/16.6/**0.8**/10.3/**1.2**/9.4/**1.6**/7.8/**1.9**/7.0/**1.9**/17.2/**3.8**/15.5, where bold numbers denote barriers and the underlined number the Si-doped quantum well with a density of 1.0×10^{17} cm^{-3} corresponding to a sheet density of 1.72×10^{11} cm^{-2}. (b) Calculated gain as a function of frequency and field strength F. (c) Frequency of the gain maximum for different values of the relative period length L/L_0 (for $x = 0.25$) and Al content x (for $L/L_0 = 1$).

5.3 THz, with the largest contribution coming from the thickness deviation.

Figure 2(a) shows the light-current density-voltage (*L-J-V*) characteristics of the sample emitting at 5.4 THz and Fig. 2(b) the corresponding emission spectra for different operating conditions. The threshold current density at low temperatures is about 275 A cm^{-2} for a 0.2×3.5 mm^2 Fabry-Pérot device increasing to 470 A cm^{-2} at the maximum operating temperature of 56 K. The operating voltage lies between 6.7 and 8.3 V. The device emits in the range of 5.37–5.43 THz with a maximum peak output power of about 6 mW at 5 K.

For the present design, we observe wafer-to-wafer variations of the center emission frequency between 4.5 and 4.8 (4.2 and 5.4) THz with (without) enabled *in-situ* thickness control,[22] where the change in frequency across a wafer is typically negligible as compared to the spectral width of the emission. We ascribe the observed wafer-to-wafer differences mainly to the sensitivity of the active-region structure to layer thicknesses variations [cf. Fig. 1(c)], which are difficult to avoid due to the technical complexity of the MBE growth of these structures. In the presence of a larger number of nominally identical samples, one can exploit this aspect to analyze general trends such as the dependence of the operating parameters on the emission frequency. Figure 3(a) shows the maximum operating temperature T_{max} as a function of the center emission frequency for more than 20 wafers of the present design type. The decrease of T_{max} with frequency is well reproduced by the linear expression $T_{max} = h(\nu_{LO} - \nu)/(ak_B) - b$, where h denotes Planck's constant, ν is the lasing frequency at the maximum operating temperature, $\nu_{LO} = 8.82$ THz the frequency of the LO phonon in GaAs at 100 K according to Ref. 23, and k_B is Boltzmann's constant. The parameters a and b are used in the fit.

One reason for the decrease of the maximum operating temperature with increasing emission frequency is the increased relaxation of electrons from the upper to the lower laser level by LO-phonon emission. Another one is the increase of optical losses at higher frequencies. To understand the first mechanism, we consider now only the two levels of the laser transition at energies E_2 and E_1 with $E_{21} = E_2 - E_1$, as indicated in the inset of Fig. 4(a). We assume that, in the unsaturated case (no stimulated emission) and at low temperatures, these levels are populated by n_2^o and n_1^o, resulting in an unsaturated population inversion $\Delta n^o = n_2^o - n_1^o$. For the moment, we will neglect intersubband scattering and assume that the electrons in the upper subband follow a Boltzmann distribution

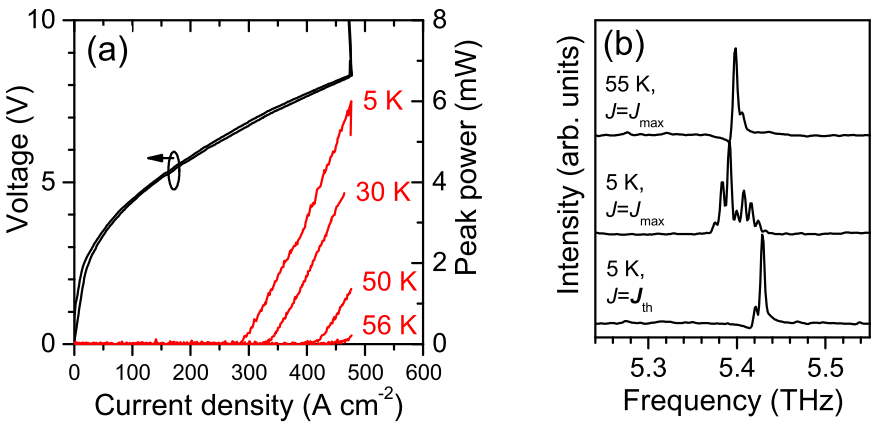

FIG. 2. (a) Measured light-current density-voltage (*L-J-V*) characteristics for a 0.2×3.5 mm^2 Fabry-Pérot QCL emitting around 5.4 THz (pulsed operation with 500 ns pulse width and 5 kHz repetition rate) for different operating temperatures. (b) Corresponding lasing spectra at threshold ($J = J_{th}$) at 5 K and maximum output power ($J = J_{max}$) at 5 and 55 K.

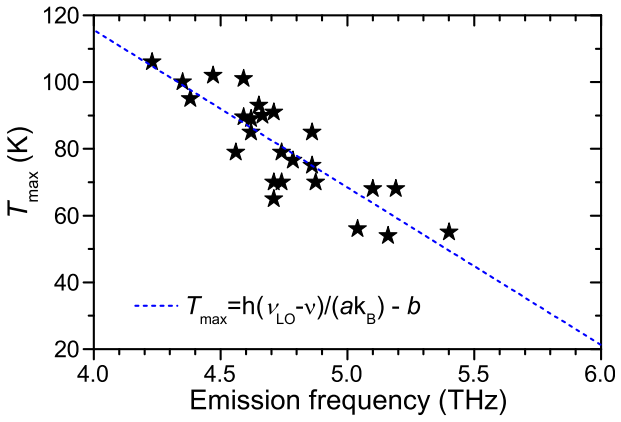

FIG. 3. Maximum operating temperature T_{max} (pulsed) vs. center emission frequency for 25 samples based on the discussed active-region design type. The dashed line represents a linear fit to the data points with parameters $a = 0.983$ and $b = 126$ K.

$$n_2 = c\int_{E_2}^{E_{max}=\infty} \exp\left(\frac{E-E_2}{k_BT}\right)dE\,, \tag{1}$$

where c is a constant prefactor, which reflects the two-dimensional density of states and the temperature-dependent chemical potential. Since integration of Eq. (1) must result in $n_2 = n_2^o$, we can write $c = n_2^o/(k_BT)$. The Boltzmann distribution is a good approximation for the Fermi-Dirac distribution, if the chemical potential is well below the subband minimum. Hence, we neglect the Fermi filling effect at very low temperatures due to the finite density of states.[24] In the next step, we take into account intersubband scattering due to LO phonons. Figure 4(a) depicts the LO-phonon scattering rate of an electron with non-negligible kinetic energy according to Ref. 25, which is virtually a step function. For comparison, the sub-threshold scattering rate from the upper to the lower laser level according to our low-temperature transport model is shown as a dashed line. Due to the strength of the Fröhlich interaction, the scattering of electrons with sufficient kinetic energy for LO-phonon emission is several orders of magnitude faster than for *cold* electrons. To account for the step function behavior, we consider now that the thermal distribution is cut at $E - E_1 = E_{LO}$, i.e., that no electrons are found in the upper subband for $E - E_1 > E_{LO}$. Integration of Eq. (1) with $E_{max} = E_1 + E_{LO}$ yields now a modified total number of electrons in each subband

$$n_2 = n_2^o - n_2^o \exp\left(\frac{E_{21}-E_{LO}}{k_BT}\right), \tag{2}$$

$$n_1 = n_1^o + n_2^o \exp\left(\frac{E_{21}-E_{LO}}{k_BT}\right). \tag{3}$$

In these equations, the parameter T corresponds to an effective temperature. We write $T = T_{lattice} + T_\Delta$, i.e., we assume that the effective temperature T is equal to the lattice temperature plus an offset T_Δ, which accounts for the temperature difference of the electron gas in the upper subband with respect to the crystal lattice. Above the maximum operating temperature T_{max} (lattice), the unsaturated population inversion becomes smaller than the required threshold inversion, $\Delta n = n_2 - n_1 < \Delta n_{th}$. At T_{max}, the difference between Δn and Δn_{th} is zero. In combination with Eqs. (2) and (3), we find that

$$T_{max} = \frac{E_{LO}-E_{21}}{k_B \ln\left[2n_2^o/(n_2^o - n_1^o - \Delta n_{th})\right]} - T_\Delta\,. \tag{4}$$

Now, we can identify the fit parameters a and b from Fig. 3(a) as $a = \ln[2n_2^o/(n_2^o - n_1^o - \Delta n_{th})]$ and $b = T_\Delta$.

For $n_1^o = 0$ and $\Delta n_{th} = 0$, we obtain the equation

$$T_{max} = \frac{E_{LO}-E_{21}}{k_B \ln(2)} - T_\Delta\,. \tag{5}$$

Since the parameter $a = 0.98$ in Fig. 3(a) is already close to $\ln(2) = 0.69$, the slope of $T_{max}(\nu)$ is not expected to change very much in future designs. However, the value of $T_\Delta = 126$ K is relatively large so that significant improvements should be obtained by reducing the electron temperature in the upper laser level.

Finally, we discuss the role of optical losses, which are subsumed in Δn_{th} in Eq. (4). Figure 4(b) depicts the

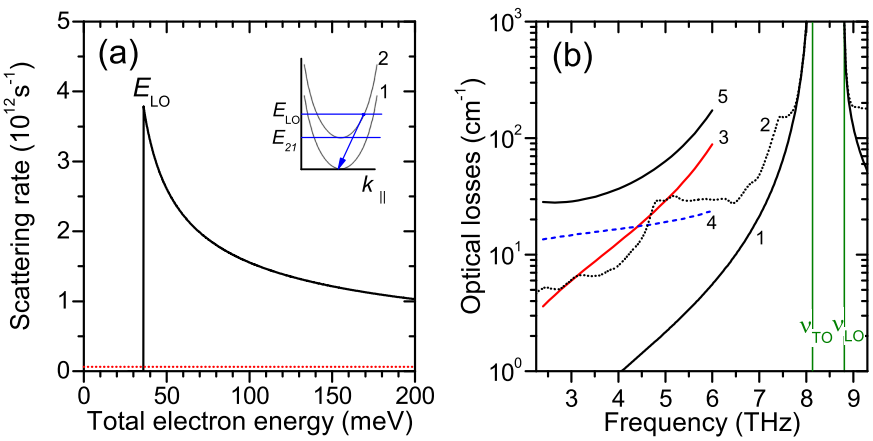

FIG. 4. (a) LO-phonon scattering rate as a function of the total electron energy (potential+kinetic) with respect to the ground level calculated according to Ref. 25 for a 25 nm wide GaAs quantum well. The dashed line indicates the scattering rate for the laser transition as obtained for our low-temperature transport model described in Ref. 16. (b) 1: optical losses due to one-phonon absorption in GaAs calculated according to Ref. 26. 2: experimentally determined optical losses for a GaAs substrate at room temperature. 3: calculated losses for a single-plasmon waveguide (infinitely long). 4: calculated losses for a metal-metal waveguide (infinitely long). 5: total losses (waveguide and mirror) for 3.5 mm-long single-plasmon cavities. ν_{LO} and ν_{TO}: frequency of the longitudinal and transverse optical phonon, respectively.

frequency dependence of the optical losses for a GaAs substrate as well as the calculated frequency dependence of the waveguide losses in a merged plot. The solid line labeled 1 indicates the losses according to one-phonon absorption in GaAs, which is a good approximation for the total losses of semi-insulating substrates at low temperatures. However, additional losses emerge at elevated temperatures due to two-phonon difference processes.[27] To illustrate the effect, the total losses as obtained from room temperature transmission measurements for semi-insulating GaAs are depicted by the dotted line labeled 2. Below 7.5 THz, two-phonon absorption clearly dominates over one-phonon absorption. Since two-phonon difference absorption is still small at 100 K, the effect of two-phonon losses should not be relevant for the present samples, but might play a role for future generations of THz QCLs. In addition, Fig. 4(b) also shows the calculated low-temperature waveguide losses for the employed single-plasmon waveguides depicted by the solid line labeled 3 as well as for metal-metal waveguides marked by the dashed line labeled 4. We obtained the data by solving the one-dimensional waveguide equation for transverse magnetic polarization considering plasma and one-phonon contributions as in Ref. 28. The parameters for the highly doped bottom contact layer have been determined by reflectance measurements for a reference sample.[29] We find that, at low temperatures, plasma losses in the metallic and quasi-metallic contact layers clearly dominate over phonon losses below 6 THz. Since metal-metal waveguides show a much smaller increase with frequency, this type of waveguide is expected to be preferable for operation above 5 THz. Although the total optical losses of the investigated single-plasmon QCLs indicated by the solid line labeled 5 in Fig. 4(b) increase substantially toward higher frequencies, the available emission range of 4.2–5.4 THz is yet too small to observe the expected change of the linear frequency dependence for T_{max} in Fig. 3(a).

In summary, we demonstrated a QCL at 5.4 THz operating in pulsed mode up to 56 K. The observed trend for the maximum operating temperature of a set of QCLs based on the same active-region type is well explained by a simple model for an additional relaxation channel by longitudinal optical phonon scattering from the upper to the lower laser level. We expect further improvements with respect to high-frequency operation by employing metal-metal waveguides instead of single-plasmon waveguides and by changing the active-region design. In particular, reducing the temperature of the electron gas in the upper laser level should lead to significantly higher operating temperatures. The development of a sufficiently fast, self-consistent simulation routine, which includes the in-plane distribution of electrons and the relevant scattering processes, will allow for the design of such active regions.

We acknowledge the expert help of M. Höricke and W. Anders with sample growth and processing, respectively. G. R. would like to thank the Deutsche Akademische Austauschdienst for an ALEARG fellowship. Part of this work was supported by the Deutsche Forschungsgemeinschaft.

[1]R. Köhler, A. Tredicucci, F. Beltram, H. E. Beere, E. H. Linfield, A. G. Davies, D. A. Ritchie, R. C. Iotti, and F. Rossi, Nature **417**, 156 (2002).
[2]H.-W. Hübers, S. G. Pavlov, H. Richter, A. D. Semenov, L. Mahler, A. Tredicucci, H. E. Beere, and D. A. Ritchie, Appl. Phys. Lett. **89**, 061115 (2006).
[3]P. Dean, Y. L. Lim, A. Valavanis, R. Kliese, M. Nikolić, S. P. Khanna, M. Lachab, D. Indjin, Z. Ikonić, P. Harrison, A. D. Rakić, E. H. Linfield, and A. G. Davies, Opt. Lett. **36**, 2587 (2011).
[4]S. Bartalini, L. Consolino, P. Cancio, P. De Natale, P. Bartolini, A. Taschin, M. De Pas, H. Beere, D. Ritchie, M. S. Vitiello, and R. Torre, Phys. Rev. X **4**, 021006 (2014).
[5]H. Richter, M. Wienold, L. Schrottke, K. Biermann, H. T. Grahn, and H.-W. Hübers, IEEE Trans. Terahertz Sci. Technol. **5**, 539 (2015).
[6]G. Scalari, C. Walther, M. Fischer, R. Terazzi, H. Beere, D. Ritchie, and J. Faist, Laser Photonics Rev. **3**, 45 (2009).
[7]C. W. I. Chan, Q. Hu, and J. L. Reno, Appl. Phys. Lett. **101**, 151108 (2012).
[8]A. J. Mayur, M. Dean Sciacca, A. K. Ramdas, and S. Rodriguez, Phys. Rev. B **48**, 10893 (1993).
[9]H.-W. Hübers, S. G. Pavlov, M. Greiner-Bär, M. H. Rümmeli, M. F. Kimmitt, R. Kh. Zhukavin, H. Riemann, and V. N. Shastin, Phys. Status Solidi B **233**, 191 (2002).
[10]S. Fathololoumi, E. Dupont, C. W. I. Chan, Z. R. Wasilewski, S. R. Laframboise, D. Ban, A. Mátyás, C. Jirauschek, Q. Hu, and H. C. Liu, Opt. Express **20**, 3866 (2012).
[11]M. Wienold, B. Röben, L. Schrottke, R. Sharma, A. Tahraoui, K. Biermann, and H. T. Grahn, Opt. Express **22**, 3334 (2014).
[12]S. Kumar, C. W. I. Chan, Q. Hu, and J. L. Reno, Nat. Phys. **7**, 166 (2011).
[13]S. Khanal, L. Zhao, J. L. Reno, and S. Kumar, J. Opt. **16**, 094001 (2014).
[14]A. Albo and Q. Hu, Appl. Phys. Lett. **106**, 131108 (2015).
[15]L. Schrottke, M. Wienold, R. Sharma, X. Lü, K. Biermann, R. Hey, A. Tahraoui, H. Richter, H.-W. Hübers, and H. T. Grahn, Semicond. Sci. Technol. **28**, 035011 (2013).
[16]L. Schrottke, M. Giehler, M. Wienold, R. Hey, and H. T. Grahn, Semicond. Sci. Technol. **25**, 045025 (2010).
[17]L. Schrottke, X. Lü, and H. T. Grahn, J. Appl. Phys. **117**, 154309 (2015).
[18]M. I. Amanti, G. Scalari, R. Terazzi, M. Fischer, M. Beck, J. Faist, A. Rudra, P. Gallo, and E. Kapon, New J. Phys. **11**, 125022 (2009).
[19]E. Luna, Á. Guzmán, A. Trampert, and G. Álvarez, Phys. Rev. Lett. **109**, 126101 (2012).
[20]X. Lü, L. Schrottke, E. Luna, and H. T. Grahn, Appl. Phys. Lett. **104**, 232106 (2014).
[21]J. Ulrich, R. Zobl, N. Finger, K. Unterrainer, G. Strasser, and E. Gornik, Physica B **272**, 216 (1999).
[22]K. Biermann, E. A. Cerda-Méndez, M. Höricke, P. V. Santos, and R. Hey, J. Cryst. Growth **323**, 56 (2011).
[23]*Handbook Series on Semiconductor Parameters*, edited by M. Levinshtein, S. Rumyantsev, and M. Shur (World Scientific, London, 1996), Vol. 1.
[24]The corresponding Fermi filling at vanishing temperature should occur up to $E_F = h^2 n_{2D}/(4\pi m^*) = 6.1$ meV above the subband minimum for a full population inversion (m^*: effective mass, $n_{2D} = 1.7 \times 10^{11}\,\mathrm{cm}^{-2}$: sheet doping density).
[25]P. Harrison, *Quantum Wells, Wires and Dots: Theoretical and Computational Physics of Semiconductor Nanostructures*, 2nd ed. (John Wiley and Sons, Chichester, 2005).
[26]*Handbook of Optical Constants of Solids*, edited by E. D. Palik (Academic Press, Orlando, 1985).
[27]E. S. Koteles and W. R. Datars, Can. J. Phys. **54**, 1676 (1976).
[28]S. Kohen, B. S. Williams, and Q. Hu, J. Appl. Phys. **97**, 053106 (2005).
[29]We found good agreement using the Drude model with a carrier density of $1.4 \times 10^{18}\mathrm{cm}^{-3}$ and a lifetime of $\tau = 0.09$ ps for the plasma term of the susceptibility.